Microsc. Microanal. 17, 206–214, 2011
doi:10.1017/S1431927610094559

Microscopy AND Microanalysis

Antibody-Mediated Self-Limiting Self-Assembly for Quantitative Analysis of Nanoparticle Surfaces by Atomic Force Microscopy

Carly Lay A. Geronimo and Robert I. MacCuspie*

Nanomechanical Properties Group, National Institute of Standards and Technology, Gaithersburg, MD, USA

Abstract: Quantification of very low density molecular coatings on large (60 nm) gold nanoparticles (AuNPs) is demonstrated via the use of antibody-mediated self-limiting self-assembly of small and large AuNPs into raspberry-like structures subsequently imaged by atomic force microscopy (AFM). AFM imaging is proposed as an automated, lower-cost, higher-throughput alternative to immunostaining and imaging by transmission electron microscopy. Synthesis of large AuNPs, containing one of three ligand molecules in one of three stoichiometries (1, 2, or 10 ligands per AuNP), and small probe AuNPs with one of three antibody molecules in a one antibody per AuNP ratio, enabled a range of predicted self-limiting self-assembled structures. A model predicting the probability of observing a given small to large AuNP ratio based on a topography measurement such as AFM is described, in which random orientational deposition is assumed and which accounts for the stochastic synthesis method of the library AuNPs with varied ligand ratios. Experimental data were found to agree very well with the predictive models when using an established AFM sample preparation method that avoids drying-induced aggregation.

Key words: self-limiting self-assembly, nanoparticle surface characterization, immunostaining, atomic force microscopy (AFM), transmission electron microscopy (TEM)

Introduction

Multifunctional nanoparticle (NP)-based therapeutics with both targeting and drug moieties have been increasingly used in clinical trials over recent years, with gold nanoparticle (AuNP) based therapeutics being just one promising example (Daniel & Astruc, 2004; Paciotti et al., 2004; Eck et al., 2008). However, one of the many key regulatory hurdles that must be addressed to facilitate approval of multifunctional AuNP-based therapeutics is the ability to quantitatively measure the composition of AuNP surfaces with single NP resolution (Hall et al., 2007; Hansen, 2008). Many integrative techniques, such as NP digestion and chemical analysis (Elghanian et al., 1997), X-ray photoelectron spectroscopy surface chemical analysis (Voevodin et al., 2007; MacCuspie et al., 2010), or dynamic light scattering (DLS) plus electrospray differential mobility analysis (Tsai et al., 2010), can provide the average number of molecules per NP. However, integrative measurements fail to provide the distribution of the coating density, i.e., whether it is a mixture of two types of NPs where one is completely functionalized and the other is entirely uncoated, a homogenous product where every NP has the average number of molecules bound, or something in between. The single NP-resolved quantification of surface coatings will provide great value in assuring quality control on batch-to-batch consistency when manufacturing these materials, reducing the risk for both patients and companies sponsoring clinical trials (Dobrovolskaia et al., 2009).

One technique that has long been fundamental to the characterization of NPs is transmission electron microscopy (TEM) (Liu, 2005; Bonevich & Haller, 2010). TEM is especially useful for characterizing colloidal AuNPs because metals scatter electrons very efficiently. However, the low electron contrast from proteins makes imaging coatings on AuNPs quite challenging. Visualization often requires the use of negative staining techniques (Ruben et al., 2005), or immunostaining, which is the labeling of antibodies (Abs) or proteins with small AuNP tags (Maeshima et al., 2005) to aid in the visualization of these low contrast materials. In the case of low density coatings, it is possible to quantify immunogenic molecules on the surface of a sufficiently large NP by using the immunostaining technique long employed by the TEM community (Williams & Carter, 2009). Stated differently, by tagging Abs with small AuNPs in a one-to-one ratio and subsequently mixing with antigen-coated large NPs, Ab-mediated self-limiting self-assembly creates raspberry-like structures, or structures with numerous smaller NPs decorating one central larger NP, which have a ratio of small to large NPs matching the ratio of antigen ligands per large NP surface. Raspberry-like hybrid NPs have been previously shown to qualitatively confirm and quantitatively approximate peptide coating densities on NP surfaces (Slocik et al., 2007; Patton et al., 2008). How-

NIST Disclaimer: Certain trade names and company products are mentioned in the text or identified in illustrations in order to specify adequately the experimental procedure and equipment used. In no case does such identification imply recommendation or endorsement by National Institute of Standards and Technology, nor does it imply that the products are necessarily the best available for the purpose.

Received August 23, 2010; accepted December 23, 2010
**Corresponding author*. E-mail: robert.maccuspie@nist.gov

ever, TEM imaging of nanostructures can be much more costly [over $1 million for TEM facilities versus on the order of $100,000 for an atomic force microscope (AFM)] and time-consuming compared to automated AFM (Neffati et al., 2003; Sitti, 2003; El Rifai & Youcef-Toumi, 2004). Additionally, automation of AFM sample loading and integration into production quality control settings is achievable with a high enough throughput to be industrially relevant, something impossible to achieve with TEM, requiring technician operation and dedicated separate offline facilities. AFM has often been employed for challenging measurements of forces and dynamics of biomolecules (Fisher et al., 1999; Yang et al., 2003; Lee et al., 2007), complex hybrid NPs (Gao et al., 2005; Zook et al., 2011), or single virus NPs (MacCuspie et al., 2008*b*), often with high degrees of spatial resolution (Ngunjiri & Garno, 2008). However, the use of AFM to image and quantify immunostained NP structures has remained quite underutilized compared to TEM (Xu et al., 2006), likely due to the complexity of interpreting a topology image compared to a transmission image and the geometrical and statistical assumptions required to successfully interpret the data (Fig. 1a, discussed later). Therefore, this work aims to develop rational physical models, based on the underlying metrology and supported by experimental datasets, for the successful quantification of low-density protein ligand coatings on NP surfaces by AFM imaging of the structures resulting from self-assembly of small NP-Ab tags onto the surface of the large NP.

Experimental

Chemicals and Reagents

Unless specified otherwise, all chemical reagents were obtained from Sigma-Aldrich (St. Louis, MO, USA) of the highest purity available and used as-received. All deionized (DI) water (resistivity of 18.2 MΩ·cm) was from an Aqua Solutions (Jasper, GA, USA) type I biological grade water purification system outfitted with an ultraviolet lamp to oxidize residual organics and a low molecular weight cut-off membrane.

Synthesis of Antibody-Functionalized AuNPs

The mechanism for attaching the Abs onto the surface of the AuNPs is shown in Figure 1b. The Abs' functions were defined as either a probe Ab if attached to the 10 nm AuNPs, or as a ligand if attached to the 60 nm AuNPs because IgG molecules can simultaneously function as Ab and antigen, and the same mechanism was used for attaching either probe Abs or ligand Abs. 1.0 mL of either nominally (i.e., in name only) 10 nm or nominally 60 nm AuNPs (Reference Materials RM8011 and RM8013, National Institute of Standards and Technology, Gaithersburg, MD, USA) were filtered through a 0.2 μm polyvinylidene fluoride syringe filter into a microcentrifuge tube (Eppendorf, Hauppauge, NY, USA). The stock AuNPs of both sizes were characterized initially under conditions used for these experiments for comparison to the informational values provided (Supplementary Materials).

Supplementary Text, Table, and Figures

Supplementary Text, Table SI-1, and Figures SI-1 to SI-8 are available online. Please visit journals.cambridge.org/jid_MAM.

However, the AuNPs used in this study were processed before measurement in a different fashion than the reference values on the National Institute of Standards and Technology (NIST) report of investigation, which accounts for the different observed values here. However, it is of note that for RM8011, the NIST report cites an AFM size of (8.5 ± 0.3) nm and a DLS size of (13.5 ± 0.1) nm, and distinct sizes between these values for the four other measurement techniques used. The measurements are statistically significant with differences well above the uncertainties of the individual measurements and reflect fundamental metrological differences between the methods. As it would be misleading to a reader to imply that the value from one single measurement is preferred among all those in the report when selecting a name for a NP (indeed multiple measurements are always best) and it would be exceedingly cumbersome to describe the NPs by all six sizes and the method used to make each measurement in every instance, the AuNPs will be referred to throughout this report by their nominal values assigned by NIST to avoid confusion. Next, 3-mercaptopropionic acid (3-MPA) was used to form an alkanethiol monolayer around the AuNPs based on stoichiometries of ligands to surface Au atoms reported in the literature (Hostetler et al., 1999; Woehrle et al., 2005; Woehrle & Hutchison, 2005; Tracy et al., 2007), and the reaction was allowed to proceed for 1 h while vortexing at speed of 115 rad s^{-1} [1,100 revolutions per minute (rpm)]. The sample was then washed by centrifugation at 14.5 krpm in a Minispin Plus (Eppendorf) for 20 min to obtain a pellet, the supernatant was removed, and then the pellet was resuspended in DI water. N-hydroxysuccinimde (NHS), then 1-ethyl-3-carbodiimide hydrochloride (EDAC) were added while the sample was vortexed at 115 rad s^{-1} (1,100 rpm) for 30 min. Affinity-purified polyclonal Abs, either Rabbit anti-Goat immunoglobulin G (IgG), Goat anti-Rabbit IgG, or Donkey anti-Rabbit IgG (Abcam, Cambridge, MA, USA) were added to the sample and allowed to react for 1 h at room temperature. The sample was washed again by centrifugation, and the pellet was resuspended in DI water as before. All samples were stored at 4°C between synthesis and measurement. Supplementary Table SI-1 shows the specified volumes and concentrations of 3-MPA, NHS, EDAC, and Abs used to create the library of materials. 60 nm AuNPs were used to produce samples with three different Ab ligand/AuNP (Lig/NP) ratios (1 Lig/NP, 2 Lig/NP, and 10 Lig/NP), and 10 nm AuNPs were used to produce three samples with 1 probe Ab/NP.

Self-Limiting Self-Assembly of Raspberry-Like Structures

Equal volumes (typically 0.5 mL each) of desired 10 and 60 nm functionalized AuNPs were mixed in a 1.5 mL low-protein binding microcentrifuge tube (Eppendorf), with approximately 100 times more 10 nm AuNPs than 60 nm AuNPs on a particle number basis, which was 10 times excess small probe AuNPs than available binding sites on the 10 Lig/NP 60 nm AuNPs. The solutions containing both sizes of AuNPs were vortexed at 94 rad s^{-1} (900 rpm) for 10 s to mix, then allowed to stand for 1 h before deposition onto AFM substrates. DLS observation of the binding kinetics (Supplementary Fig. SI-1) suggests reactions were complete after 20 min.

Dynamic Light Scattering and Ultraviolet-Visible Absorbance Characterization

NIST-NCL Protocol PCC-1 was followed (Hackley & Clogston, 2007). Briefly, samples were transferred into a disposable ultraviolet-transparent semimicro cuvette (BrandTech Scientific, Inc., Essex, CT, USA) to measure the hydrodynamic diameter (Z_{avg}) on a ZetaSizer Nano (Malvern Instruments, Westborough, MA, USA). For this article, DLS data will be reported as the mean of five measurements with one standard deviation uncertainty. On completion of the DLS measurements, the cuvette was immediately transferred to a Lambda 750 Spectrophotometer (Perkin Elmer, Waltham, MA, USA) for ultraviolet-visible (UV-vis) spectra collection.

AFM Sample Preparation and Imaging

NIST-NCL Protocol PCC-6 was followed (Grobleny et al., 2009). All sample preparation was performed in a HEPA-filtered biosafety level two (BSL-2) hood. Briefly, preparation of substrate: 0.1% by mass poly-*L*-Lysine (PLL) solution was diluted 1:10 with filtered DI water. Freshly cleaved mica discs (Ted Pella, Redding, CA, USA) were fully immersed in PLL solution for 30 min at room temperature, removed from the solution, rinsed with DI water, and dried with filtered compressed air. Deposition of AuNPs onto substrate: 25 μL of solution was pipetted onto a PLL-modified substrate and incubated (10 nm AuNP for 30 s; 60 nm AuNP or raspberry-like structures for 10 min) at room temperature under an inverted glass petri dish cover to minimize evaporation, then the droplet was rinsed away with DI water and dried with filtered compressed air as before. This protocol deposits NPs in a way that minimizes drying-induced aggregation or agglomeration artifacts, or the so-called "coffee stain effect," and reduces radial dependence of NP distribution on the substrate (although not explored systematically in this report, see NIST-NCL Protocols PCC-6 and PCC-7). A Dimension 3100 scanning probe microscope and Nanoscope V Controller (Bruker AXS, Santa Barbara, CA, USA) equipped with an automated stage was operated in intermittent-contact mode with scan rates of 0.9 Hz. No fewer than 10 images were collected at arbitrary locations across a sample using an automated programmed move routine to collect either 60 or 100 images in one session; one tip was used per session then discarded. Image collection through programmed moves was repeated until at least 100 large NPs were imaged; however, in most cases, only one tip was needed per sample. Tip shape, wear, and contamination were assessed by imaging nominally 30 nm citrate capped AuNPs on the first image collected with a fresh tip and every tenth image, using a previously described method (Markiewicz & Goh, 1994), described in detail in the Supplementary Materials and Supplementary Figure SI-2, as well as by examining for repetitive image artifacts indicative of contamination or tip damage, as shown in Supplementary Figure SI-3. Figures shown are the most representative of all data observed. Histograms were prepared by visual analysis of the structures imaged by the user, with examples of how small to large NP ratios were assigned displayed in Supplementary Figures SI-4 to SI-7. A subset of structures were analyzed using the cross-section analysis tool of the Nanoscope v7.20 software and manually selecting a point on the substrate surface and a point at the peak of the small or large NP in the structure, and an example screenshot of such an analysis is shown in Supplementary Figure SI-8. A tolerance for size changes due to the surface chemistry reactions and subsequent processing was kept in mind when measuring the small and large NPs.

Results and Discussion

This work first focused on creating well-defined ligand-functionalized AuNPs and probe-Ab-functionalized AuNPs to later create the self-limiting self-assembled (S-L S-A) raspberry-like structures needed to test the main hypothesis. Abs were selected as the ligands because they have been explored for targeting specific cellular receptors to facilitate uptake of AuNPs preferentially in certain tissues or cell types, can simultaneously act as both antigens and Abs, and can demonstrate the potential applicability of this approach to sandwich immunoassay techniques. 60 nm AuNPs were used to produce samples with three different Lig/NP ratios of (1, 2, or 10) Lig/NP (Jiang et al., 2004). All of the 10 nm AuNPs were engineered with the stoichiometric ratio less than 1 Ab/NP to assure high yield of only 1 Ab/NP products in this stochastic reaction (Shaffer et al., 2004; Worden et al., 2004), for the purposes of controlling the subsequent self-assembly (Fig. 1c) in a self-limiting fashion to prevent bridging of multiple large AuNP per small AuNP (Fig. 1d). Selection of antibodies was made that would provide combinations of complimentary recognition (Rabbit anti-Goat IgG plus Goat anti-Rabbit IgG), singular recognition (Donkey anti-Rabbit IgG plus Rabbit anti-Goat IgG), and no recognition (Goat anti-Rabbit IgG plus Donkey anti-Rabbit IgG). These combinations are illustrated in Figure 1e.

The Ab-functionalized AuNPs were then characterized by integrative techniques to confirm the conjugation of the Abs onto the surfaces of the AuNPs. Figure 2a shows the DLS Z_{avg} size measurements of 60 nm AuNPs before and

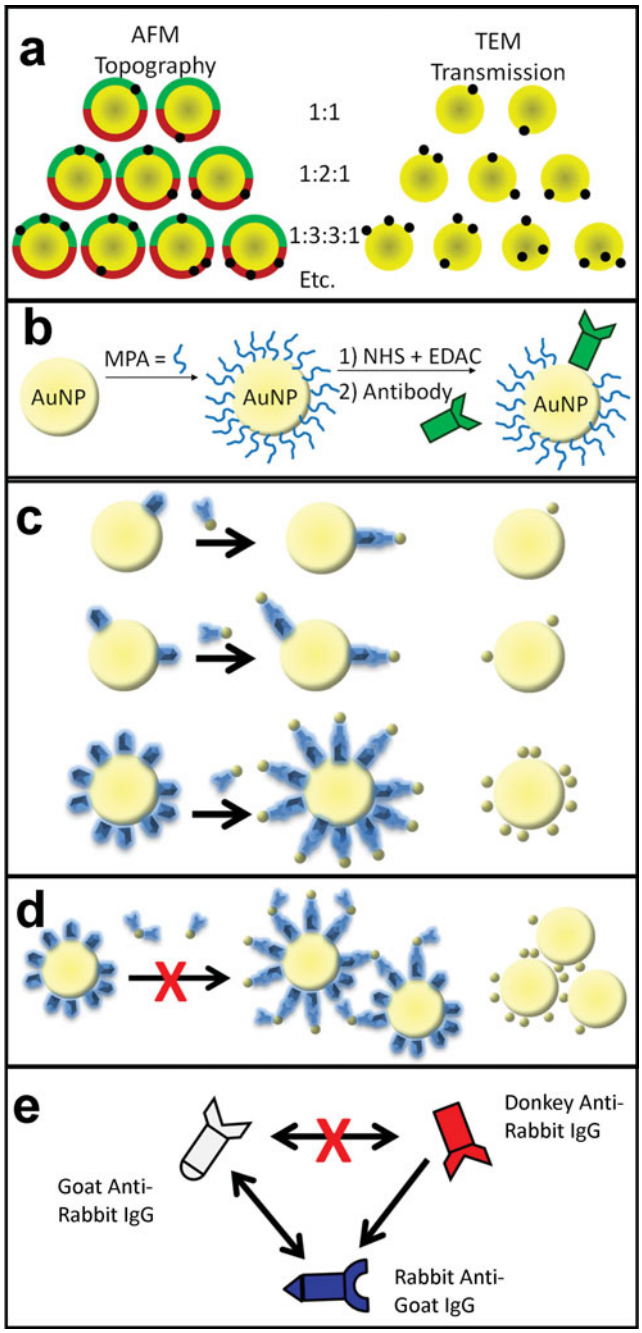

Figure 1. a: (Left) Green-shaded regions highlight areas on the large AuNP where small AuNPs could be imaged successfully by a topographic measurement technique such as AFM, with the frequency of occurrence based on random probabilities in the center; (Right) examples of how each structure on the left may appear by a transmission measurement technique such as TEM. **b:** Reaction scheme for the attachment of Abs onto the surface of AuNPs (applicable to any amine-containing ligand), using 3-mercaptopropionic acid (MPA), N-hydroxysuccinimide (NHS), 1-ethyl-3-carbodiimide hydrochloride (EDAC), and the desired antibody (Ab). **c:** 10 nm AuNPs self-assembled onto 60 nm AuNPs depending on complimentary pairings of Abs and the Lig/NP ratio; the Ab/NP ratio for 10 nm AuNPs was 1:1, enabling S-L S-A into the raspberry-like structures as shown and avoiding (**d**) uncontrolled growth of large and small AuNP networks. **e:** Recognition interactions of the different antibody-antigen combinations employed in this work.

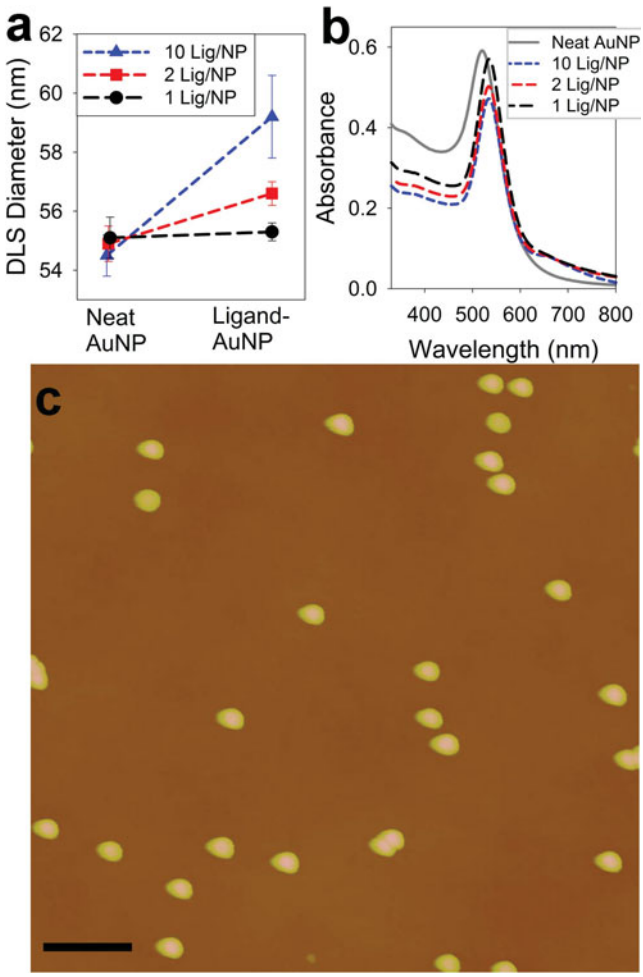

Figure 2. Characterization of Ligand-AuNP conjugates. (**a**) DLS size measurements of 60 nm AuNP pre- and post-conjugation with Donkey anti-Rabbit IgG at (1, 2, and 10) Lig/NP, (**b**) UV-Vis spectrum of neat citrate 60 nm AuNPs and (1, 2, and 10) Lig/NP 60 nm AuNPs, and (**c**) AFM height image of 60 nm AuNP with 1 Lig/NP Goat anti-Rabbit IgG. Scale bar represents 500 nm. *Z* color scale is 125 nm.

after conjugation with the Donkey anti-Rabbit IgG for all three Lig/NP ratios. These small increases in diameter are reasonable when one considers the additional hydrodynamic volume of 1 or even 10 Abs is much smaller than that of a 60 nm AuNP, and that the Z_{avg} diameter increases only by the cube root of this (see Supplementary Materials for further calculation details). While the increase from neat-AuNPs to Ligand-AuNPs in Figure 2a is larger than predicted from the calculations described in the Supplementary Materials, this is likely due to water molecules associating with the antibody coatings, increasing the hydrodynamic volume and/or hydrodynamic drag of the Ligand-AuNP more than a solely geometric assumption would calculate. Indeed, this effect has been observed experimentally, for example, by Tsai and others, with other hydrophilic coatings (Tsai et al., 2010). The size increase was less than the uncertainty of the measurements for 1 Lig/NP, small but approaching statistical significance (approximately 2 nm

increase) for 2 Lig/NP, and clearly significant (almost 5 nm) for 10 Lig/NP. The greater size changes observed for greater Lig/NP ratios agrees with the solution chemistry stoichiometry increases but does not rigorously confirm the binding of the Abs or the precise Lig/NP ratio of the surface attachment. The standard deviation of the mean of the *Z*-average DLS measurements in Figure 2a for the Ligand-AuNPs is likely due to the polydispersity of the NPs' surface coatings (i.e., particles made with a 10:1 stoichiometry actually yield a wide distribution of coating ratios due to the stochastic nature of the reaction). The DLS results for Donkey anti-Rabbit IgG are representative of the other Abs used (Rabbit anti-Goat IgG or Goat anti-Rabbit IgG).

The unique optical properties of AuNPs enable both concentration quantification and qualitative monitoring of changes in the surface coating (Link & El-Sayed, 1999; Malinsky et al., 2001; Kelly et al., 2002; Duan et al., 2009). Figure 2b shows the UV-vis spectrum of the 60 nm citrate-capped AuNP control with a maximum absorbance near 520 nm and the UV-vis spectrum of 60 nm AuNP-Goat anti-Rabbit IgG (2 Lig/NP) with a maximum absorbance observed near a wavelength of 530 nm. This slight red shift suggests that a coating is present on the surface of the AuNPs, here the Abs. Decreases in absorbance allow quantification of the yield of the reaction and purification steps. The UV-vis result shown is representative of the other Ab samples.

Figure 2c shows topographical AFM images of 60 nm AuNP-Rabbit anti-Goat IgG (1 Lig/NP). The majority of structures observed in the AuNP stocks are single NPs, with very little agglomeration. The size increase by DLS combined with the AFM result of single AuNPs strongly suggests that the AuNPs have been surface functionalized. Within an individual AuNP structure, a region of phase contrast can sometimes be observed, indicating perhaps a more compliant material is present in only a small region of the NP surface, also suggesting the presence of a functionalized Ab. However, caution must be exercised to avoid overinterpretation of AFM phase images. When viewed collectively, the DLS, AFM, and UV-vis measurements suggest increasing ligand protein density on the surface of the AuNPs matching the trend of the solution stoichiometries used during synthesis. This combination of integrative techniques has been previously demonstrated as qualitatively valid to observe protein coatings on AuNPs and AgNPs and distinguish agglomerates or aggregates from singly dispersed protein-coated NPs (Nuraje et al., 2006; MacCuspie et al., 2011). While these combined integrative size measurements confirm the ability to control the average protein coating density on the surface of the AuNPs, unfortunately the precise quantities of ligands bound to each single NP are impossible to determine by any integrative technique.

After synthesizing the library of Ab-NP conjugates, the Ab-mediated S-L S-A of the smaller AuNPs onto the larger AuNPs forming raspberry-like structures was performed as illustrated in Figure 1c. Without the self-limiting feature of only one probe Ab per small AuNP, uncontrolled large agglomerated networks (see Supplementary Materials for a discussion on terminology selection) of target Lig-AuNPs and probe Ab-AuNPs would be formed (Fig. 1d) similar to previously reported peptide nanotubes biosensor networks (MacCuspie et al., 2008*a*). The AuNPs self-assemble depending on the reactivity of the Abs and the number of Abs on the large AuNPs. For instance, both Rabbit anti-Goat IgG and Goat anti-Rabbit IgG express affinity for one another; Donkey anti-Rabbit IgG expresses an affinity for Rabbit anti-Goat IgG, and Goat anti-Rabbit and Donkey anti-Rabbit express no affinity for one another.

Quantifying the number of self-assembled NPs of various small to large NP ratios based on an AFM image alone can be challenging or even misleading without careful consideration of the fundamental physics of the metrology involved. Thus, a rational model was developed to aid in the interpretation of the data (Fig. 1a). The key assumptions of the model are as follows: (1) random orientation of Ab attachment onto large AuNPs, and thus small AuNPs will assemble onto the large AuNPs with random orientations relative to one another on the particle surface, (2) the S-L S-A structures will deposit with random orientations onto AFM imaging substrates, (3) as the AFM technique images topography, only those small AuNPs that are oriented on the top half of the large AuNP post-deposition onto the AFM imaging substrate will be counted as illustrated in Figure 1a (for example, if one small AuNP attaches to one large AuNP, there is a 50% chance that the presence of the small AuNP will be imaged, illustrated such that only the small AuNPs attached to the green region of the large AuNPs would be imaged and any small AuNPs bound to the red region would not be imaged), and (4) a distribution of Lig/NP products with a mean of the expected value and a standard deviation of 1, due to the stochastic nature of using solution-driven stoichiomety to control the synthesis of the products (Levy et al., 2006).

The imaging substrate sample prep methods used have been proven to prevent drying-induced aggregation of AuNPs for both AFM and TEM work (NIST, 2008; ASTM, 2009; Grobleny et al., 2009; Bonevich & Haller, 2010), and were further demonstrated using the single AuNP control samples shown in Figure 2c. Figure 3 shows the resulting concentration dependence of the raspberry-like structures from a series of S-L S-A reactions with predicted (0, 1, 2, or 10) small to large NP ratios. The reactions were between 10 nm AuNP-Goat anti-Rabbit IgG (1 Ab/NP) and 60 nm AuNP-Rabbit anti-Goat IgG with (1, 2, or 10) Lig/NP. The sample labeled 0 was an Ab-autoaffinity control reaction of 10 nm AuNP-Rabbit anti-Goat IgG (1 Ab/NP) and the 60 nm AuNP-Rabbit anti-Goat IgG with 1 Lig/NP because the Ab should not recognize itself as an antigen unless there is an autoaffinity, and thus the predicted small to large NP ratio is 0. The images in the left column are representative of various small to large NP ratios observed for the raspberry-like structures. The histograms represent the total number of structures observed from no less than 10 AFM height

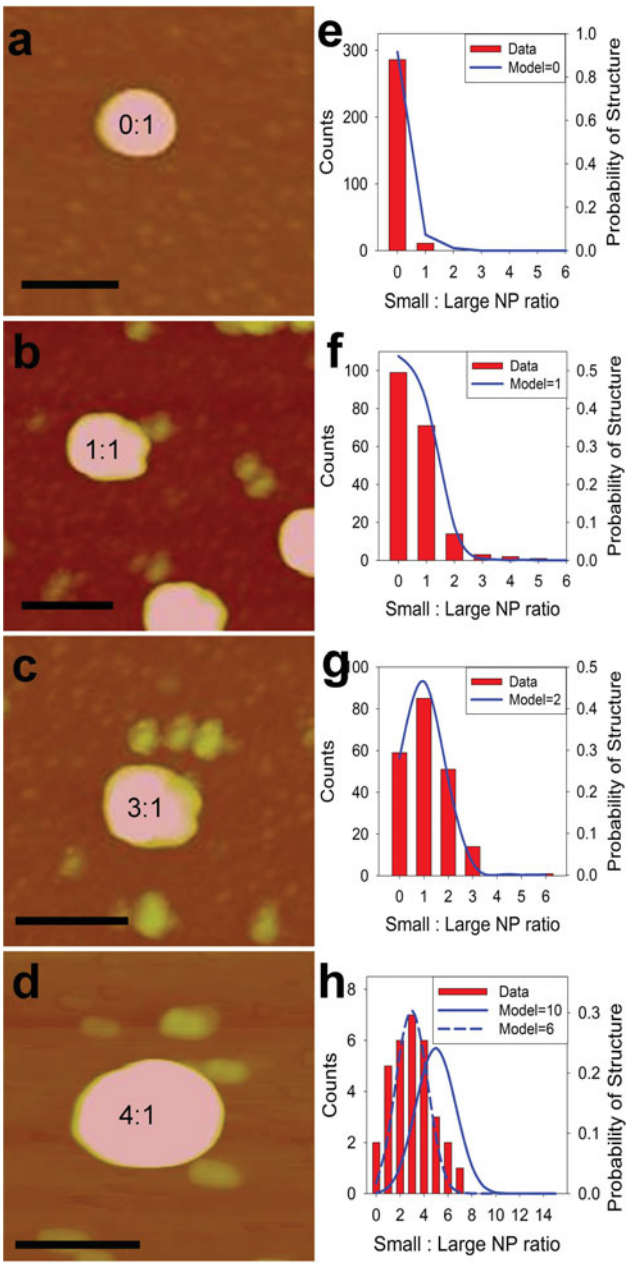

Figure 3. Lig/NP concentration series. Representative AFM height images (**a–d**) showing example raspberry-like S-L S-A AuNP structures with small to large AuNP ratios labeled, and histograms (**e–h**) of the small to large NP ratio observed for the self-assembly of 10 nm AuNPs with Goat anti-Rabbit IgG onto 60 nm AuNPs with Rabbit anti-Goat IgG in (**e**) autoaffinity negative control, (**f**) 1 Lig/NP, (**g**) 2 Lig/NP, and (**h**) 10 Lig/NP surface concentrations. For the histograms, red bars are data and blue lines are predicted values based on calculations using the model with mean values inputted identified in the legends. Scale bars are 100 nm. *Z* color scale is set to 40 nm to allow easier visualization of the 10 nm AuNPs.

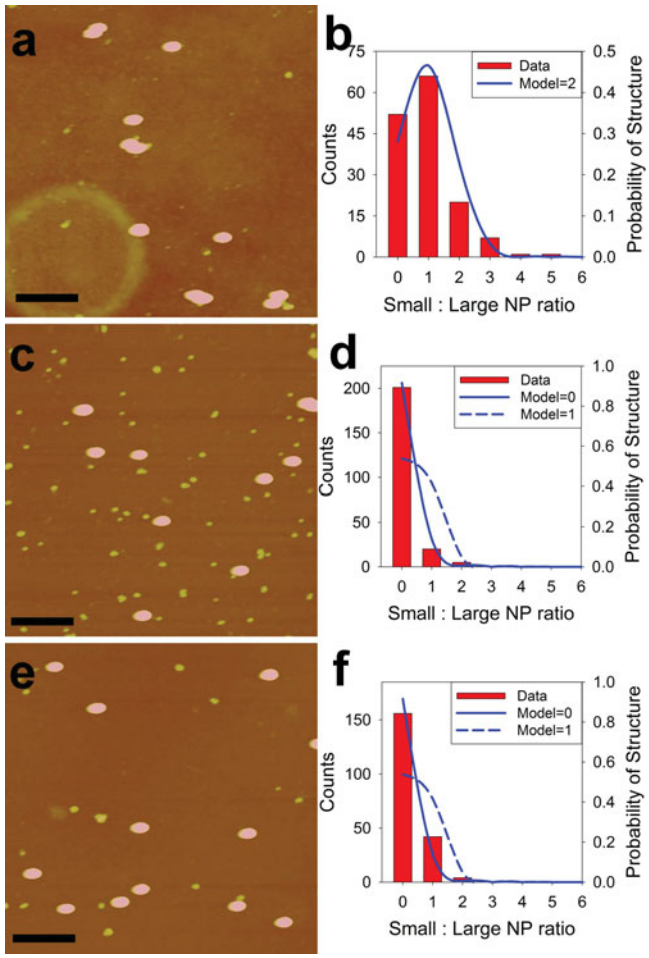

Figure 4. Antibody specificity series. Representative AFM height images (**a, c, e**) and histograms (**b, d, f**) of the small to large NP ratio observed for the self-assembly of small AuNPs with Goat anti-Rabbit IgG onto large AuNPs with 2 Lig/NP of (**a, b**) Rabbit anti-Goat IgG, (**c, d**) Donkey anti-Rabbit IgG, and (**e, f**) Goat anti-Rabbit IgG. For the histograms, red bars are data and blue lines are predicted values based on the model with mean values inputted identified in the legends. Scale bars represent 500 nm. *Z* color scale is set to 40 nm to allow easier visualization of the 10 nm AuNPs.

images (example images used to create the histograms, with small to large NP ratio assignments labeled, can be found in Supplementary Figures SI-4 to SI-7). The predicted probability of structures observed, based on a predicted mean from the solution stoichiometry and a standard deviation of one, is overlaid on the histograms.

The negative control, or 0 Lig/NP, shows that the AuNP concentrations and sample preparation procedures used leads to less than 4% occurrence of false-positive structures, likely due as much or more to the Abs' autoaffinity than to sample preparation. For (0, 1, and 2) Lig/NP, the model fits the data very well (Fig. 3e–g). However, in the case of 10 Lig/NP (Fig. 3h), the sample appears to exceed the upper bound of detection for the technique, as the model for 6 Lig/NP provides a much better fit to the data than the model for 10 Lig/NP, likely due to a breakdown in the assumptions that there is no steric hindrance in either the ligand coupling reaction or the S-L S-A, a reasonable assumption considering that no structures were observed that contained over eight small AuNPs per large AuNP. It is

also possible that asymmetrical raspberries may deposit preferentially with the side containing more small AuNPs facing the AFM substrate. The 10 Lig/NP results highlight not only the limitations for quantifying high coating densities, but also the power of this technique to examine extremely low ligand coating densities on NP surfaces with single NP resolution.

To further reinforce the specificity afforded by using Ab-mediated self-assembly (Nuraje et al., 2004), a series of ligands that were either complimentary or noncomplimentary to the probe Ab were examined. Figure 4 summarizes representative AFM height images and histograms of the small to large NP ratios of the structures observed for this series. Figure 4a,b is the complimentary pair, 10 nm AuNP-Goat anti-Rabbit IgG (1 Ab/NP) and 60 nm AuNP-Rabbit anti-Goat IgG with 2 Lig/NP. The model for 2 Lig/NP fits the data reasonably well, suggesting that perhaps the mean was slightly less than two. The low-height rings in Figure 4a and Supplementary Figure SI-7 are likely inhomogeneities from preparing the PLL coating on the mica. For the case of the noncomplimentary pairings of 2 Lig/NP 60 nm AuNPs, Donkey anti-Rabbit IgG or Goat anti-Rabbit IgG were used in Figures 4c–d and 4e,f, respectively. While there was a slightly greater than expected frequency of false positives, it was still well below the model prediction for an average 1 Lig/NP structure, demonstrating this immunostaining approach of using probe Abs tagged with single AuNPs and AFM imaging is valid.

Conclusions

The method of employing Ab-mediated S-L S-A followed by subsequent imaging of the raspberry-like structures by AFM was developed here for quantitative measurements of low density coatings of biomolecules on NP surfaces with single NP statistics. A library of large AuNPs with varied Lig/NP ratios and different complimentary and noncomplimentary small probe-Ab AuNPs were synthesized and characterized by both integrative methods and AFM imaging to provide histograms of the observed small to large NP ratios in the raspberry-like structures. A rational physical model based on the underlying metrology was developed to aid in the quantitative interpretation of a topographic measurement, which was found to agree especially well with the experimental data at very low Lig/NP ratios, for example (0, 1, or 2) Lig/NP.

The model enables use of AFM to confirm S-L S-A and quantitative measurements of the NPs' surfaces. Visual analysis of the self-assembled NPs, which could later be automated by image processing software for further efficiency gains, provides easier interpretation of results compared to more complicated AFM force curve mechanical property measurements. This method fills a critical gap in measurement approaches by providing a high number of single NP measurements in a potentially highly automated fashion.

Future work could explore the S-L S-A of smaller probe AuNPs to understand the role steric hindrance may play in the S-L S-A process, perhaps expanding the quantitative range of Lig/NP ratios by using smaller probe AuNPs. In this work (10 and 60) nm AuNPs were selected because of their availability as reference materials. Alternatively, in principal this work could also be expanded beyond Abs to use many other complimentary biomolecule-driven recognition such as aptamers, biotin-avidin, or affinity peptides. Nevertheless, this AFM-based method can now be used to provide evidence with single NP resolution that low-density coatings are in fact uniformly distributed across all the NPs in a sample, a key enabling step to ensuring batch-to-batch consistency in regulated environments such as pharmaceutical companies developing NP-based drug delivery systems and therapies where the number of drug or targeting molecules per NP can play an important role the cellular uptake, fate, and transport of the NP.

Acknowledgments

C.L.A.G. was supported in part by the National Science Foundation's Research Experience for Undergraduates (REU) program, Division of Materials Research. The authors also acknowledge Julian Taurozzi, Robert Cook, and Justin Gorham for their critical review of the manuscript.

References

ASTM (2009). Interlaboratory Study to Establish Precision Statements for ASTM E2490-09 Standard Guide for measurement of particle size distribution of nanomaterials in suspension by photon correlation spectroscopy. Research Report E56-1001. West Conshohocken, PA: American Society for Testing and Materials.

Bonevich, J.E. & Haller, W.K. (2010). NIST—NCL Joint Assay Protocol, PCC-7: Measuring the size of nanoparticles using transmission electron microscopy (TEM). Gaithersburg, MD: National Institute of Standards and Technology.

Daniel, M.C. & Astruc, D. (2004). Gold nanoparticles: Assembly, supramolecular chemistry, quantum-size-related properties, and applications toward biology, catalysis, and nanotechnology. *Chem Rev* **104**, 293–346.

Dobrovolskaia, M.A., Patri, A.K., Zheng, J.W., Clogston, J.D., Ayub, N., Aggarwal, P., Neun, B.W., Hall, J.B. & McNeil, S.E. (2009). Interaction of colloidal gold nanoparticles with human blood: Effects on particle size and analysis of plasma protein binding profiles. *Nanomed-Nanotechnol Biol Med* **5**, 106–117.

Duan, J., Park, K., MacCuspie, R.I., Vaia, R.A. & Pachter, R. (2009). Optical properties of rodlike metallic nanostructures: Insight from theory and experiment. *J Phys Chem C* **113**, 15524–15532.

Eck, W., Craig, G., Sigdel, A., Ritter, G., Old, L.J., Tang, L., Brennan, M.F., Allen, P.J. & Mason, M.D. (2008). PEGylated gold nanoparticles conjugated to monoclonal F19 antibodies as targeted labeling agents for human pancreatic carcinoma tissue. *ACS Nano* **2**, 2263–2272.

Elghanian, R., Storhoff, J.J., Mucic, R.C., Letsinger, R.L. & Mirkin, C.A. (1997). Selective colorimetric detection of polynucleotides based on the distance-dependent optical properties of gold nanoparticles. *Science* **277**, 1078–1081.

El Rifai, O.M. & Youcef-Toumi, K. (2004). On automating atomic force microscopes: An adaptive control approach. *Proceedings 43rd IEEE Conference on Decision and Control (CDC)*, Vols. 1–5, pp. 1574–1579. New York: Institute of Electrical and Electronics Engineers.

Fisher, T.E., Oberhauser, A.F., Carrion-Vazquez, M., Marszalek, P.E. & Fernandez, J.M. (1999). The study of protein mechanics with the atomic force microscope. *Trends Biochem Sci* **24**, 379–384.

Gao, X.Y., Yu, L.T., MacCuspie, R.I. & Matsui, H. (2005). Controlled growth of Se nanoparticles on Ag nanoparticles in different ratios. *Adv Mater* **17**, 426–429.

Grobleny, J., Delrio, F.W., Pradeep, N., Kim, D.-I., Hackley, V.A. & Cook, R.F. (2009). NIST—NCL Joint Assay Protocol, PCC-6: Size measurement of nanoparticles using atomic force microscopy. Gaithersburg, MD: National Institute of Standards and Technology. Available at http://ncl.cancer.gov/working_assay-cascade.asp.

Hackley, V.A. & Clogston, J.D. (2007). NIST—NCL Joint Assay Protocol PCC-1: Measuring the size of nanoparticles in aqueous media using batch-mode dynamic light scattering. Gaithersburg, MD: National Institute of Standards and Technology.

Hall, J.B., Dobrovolskaia, M.A., Patri, A.K. & McNeil, S.E. (2007). Characterization of nanoparticles for therapeutics. *Nanomedicine* **2**, 789–803.

Hansen, D.J. (2008). FDA confronts nanotechnology. *Chem Eng News* **86**, 32–34.

Hostetler, M.J., Templeton, A.C. & Murray, R.W. (1999). Dynamics of place-exchange reactions on monolayer-protected gold cluster molecules. *Langmuir* **15**, 3782–3789.

Jiang, K.Y., Schadler, L.S., Siegel, R.W., Zhang, X.J., Zhang, H.F. & Terrones, M. (2004). Protein immobilization on carbon nanotubes via a two-step process of diimide-activated amidation. *J Mater Chem* **14**, 37–39.

Kelly, K.L., Coronado, E., Zhao, L.L. & Schatz, G.C. (2002). The optical properties of metal nanoparticles: The influence of size, shape, and dielectric environment. *J Phys Chem B* **107**, 668–677.

Lee, C.K., Wang, Y.M., Huang, L.S. & Lin, S.M. (2007). Atomic force microscopy: Determination of unbinding force, off rate and energy barrier for protein-ligand interaction. *Micron* **38**, 446–461.

Levy, R., Wang, Z.X., Duchesne, L., Doty, R.C., Cooper, A.I., Brust, M. & Fernig, D.G. (2006). A generic approach to monofunctionalized protein-like gold nanoparticles based on immobilized metal ion affinity chromatography. *Chembiochem* **7**, 592–594.

Link, S. & El-Sayed, M.A. (1999). Spectral properties and relaxation dynamics of surface plasmon electronic oscillations in gold and silver nanodots and nanorods. *J Phys Chem B* **103**, 8410–8426.

Liu, J.Y. (2005). Scanning transmission electron microscopy and its application to the study of nanoparticles and nanoparticle systems. *J Elec Microsc* **54**, 251–278.

MacCuspie, R.I., Allen, A.J. & Hackleky, V.A. (2011). Dispersion stabilization of silver nanoparticles in synthethetic lung fluid studied under in-situ conditions. *Nanotoxicology* doi:10.3109/17435390.2010.504311.

MacCuspie, R.I., Banerjee, I.A., Pejoux, C., Gummalla, S., Mostowski, H.S., Krause, P.R. & Matsui, H. (2008*a*). Virus assay using antibody-functionalized peptide nanotubes. *Soft Matter* **4**, 833–839.

MacCuspie, R.I., Elsen, A.M., Diamanti, S.J., Patton, S.T., Altfeder, I., Jacobs, J.D., Voevodin, A.A. & Vaia, R.A. (2010). Purification—chemical structure—electrical property relationship in gold nanoparticle liquids. *Appl Organometal Chem* **24**, 590–599.

MacCuspie, R.I., Nuraje, N., Lee, S.Y., Runge, A. & Matsui, H. (2008*b*). Comparison of electrical properties of viruses studied by AC capacitance scanning probe microscopy. *J Am Chem Soc* **130**, 887–891.

Maeshima, K., Eltsov, M. & Laemmli, U.K. (2005). Chromosome structure: Improved immunolabeling for electron microscopy. *Chromosoma* **114**, 365–375.

Malinsky, M.D., Kelly, K.L., Schatz, G.C. & Van Duyne, R.P. (2001). Chain length dependence and sensing capabilities of the localized surface plasmon resonance of silver nanoparticles chemically modified with alkanethiol self-assembled monolayers. *J Am Chem Soc* **123**, 1471–1482.

Markiewicz, P. & Goh, M.C. (1994). Atomic force microscopy probe tip visualization and improvement of images using a simple deconvolution procedure. *Langmuir* **10**, 5–7.

Neffati, R., Alexeev, A., Saunin, S., Brokken-Zijp, J.C.M., Wouters, D., Schmatloch, S., Schubert, U.S. & Loos, J. (2003). Automated scanning probe microscopy as a new tool for combinatorial polymer research: Conductive carbon black/poly(dimethylsiloxane) composites. *Macromolec Rapid Comm* **24**, 113–117.

Ngunjiri, J. & Garno, J.C. (2008). AFM-based lithography for nanoscale protein assays. *Anal Chem* **80**, 1361–1369.

NIST (2008). Reference Material 8011, Gold Nanoparticles, Nominal 10 nm diameter. Gaithersburg, MD: National Institute of Standards and Technology.

Nuraje, N., Banerjee, I.A., Maccuspie, R.I., Yu, L.T. & Matsui, H. (2004). Biological bottom-up assembly of antibody nanotubes on patterned antigen arrays. *J Am Chem Soc* **126**, 8088–8089.

Nuraje, N., Su, K., Samson, J., Haboosheh, A., MacCuspie, R.I. & Matsui, H. (2006). Self-assembly of Au nanoparticle-containing peptide nano-rings on surfaces. *Supramolec Chem* **18**, 429–434.

Paciotti, G.F., Myer, L., Weinreich, D., Goia, D., Pavel, N., McLaughlin, R.E. & Tamarkin, L. (2004). Colloidal gold: A novel nanoparticle vector for tumor directed drug delivery. *Drug Delivery* **11**, 169–183.

Patton, S.T., Slocik, J.M., Campbell, A., Hu, J.J., Naik, R.R. & Voevodin, A.A. (2008). Bimetallic nanoparticles for surface modification and lubrication of MEMS switch contacts. *Nanotechnology* **19**, 405705–405711.

Ruben, G.C., Wang, J.Z., Iqbal, K. & Grundke-Iqbal, I. (2005). Paired helical filaments (PHFs) are a family of single filament structures with a common helical turn period: Negatively stained PHF imaged by TEM and measured before and after sonication, deglycosylation, and dephosphorylation. *Microsc Res Techniq* **67**, 175–195.

Shaffer, A.W., Worden, J.G. & Huo, Q. (2004). Comparison study of the solution phase versus solid phase place exchange reactions in the controlled functionalization of gold nanoparticles. *Langmuir* **20**, 8343–8351.

Sitti, M. (2003). Teleoperated and automatic nanomanipulation systems using atomic force microscope probes. *Proceedings 42nd IEEE Conference on Decision and Control*. Vols. 1–6, pp. 2118–2123. New York: Institute of Electrical and Electronics Engineers.

Slocik, J.M., Tam, F., Halas, N.J. & Naik, R.R. (2007). Peptide-assembled optically responsive nanoparticle complexes. *Nano Lett* **7**, 1054–1058.

Tracy, J.B., Kalyuzhny, G., Crowe, M.C., Balasubramanian, R., Choi, J.P. & Murray, R.W. (2007). Poly(ethylene glycol) ligands for high-resolution nanoparticle mass spectrometry. *J Am Chem Soc* **129**, 6706–6707.

Tsai, D.-H., Delrio, F.W., MacCuspie, R.I., Cho, T.J., Zachariah, M. & Hackley, V.A. (2010). Competitive adsorption of thiolated polyethylene glycol and mercaptopropionic acid on gold nanoparticles measured by physical characterization methods. *Langmuir* **26**, 10325–10333.

Voevodin, A.A., Vaia, R.A., Patton, S.T., Diamanti, S., Pender, M., Yoonessi, M., Brubaker, J., Hu, J.J., Sanders, J.H., Phillips, B.S. & MacCuspie, R.I. (2007). Nanoparticte-wetted surfaces for relays and energy transmission contacts. *Small* **3**, 1957–1963.

Williams, D.B. & Carter, C.B. (2009). *Transmission Electron Microscopy: A Textbook for Materials Science*. New York: Springer Science.

Woehrle, G.H., Brown, L.O. & Hutchison, J.E. (2005). Thiol-functionalized, 1.5-nm gold nanoparticles through ligand exchange reactions: Scope and mechanism of ligand exchange. *J Am Chem Soc* **127**, 2172–2183.

Woehrle, G.H. & Hutchison, J.E. (2005). Thiol-functionalized undecagold clusters by ligand exchange: Synthesis, mechanism, and properties. *Inorganic Chem* **44**, 6149–6158.

Worden, J.G., Dai, Q., Shaffer, A.W. & Huo, Q. (2004). Monofunctional group-modified gold nanoparticles from solid phase synthesis approach: Solid support and experimental condition effect. *Chem Mater* **16**, 3746–3755.

Xu, X.Y., Rosi, N.L., Wang, Y.H., Huo, F.W. & Mirkin, C.A. (2006). Asymmetric functionalization of gold nanoparticles with oligonucleotides. *J Am Chem Soc* **128**, 9286–9287.

Yang, Y., Wang, H. & Erie, D.A. (2003). Quantitative characterization of biomolecular assemblies and interactions using atomic force microscopy. *Methods* **29**, 175–187.

Zook, J.M., MacCuspie, R.I., Locascio, L.E. & Elliott, J.E. (2011). Stable nanoparticle aggregates/agglomerates of different sizes and the effect of their sizes on hemolytic cytotoxicity. *Nanotoxicology* doi:10.3109/17435390.2010.536615.